Marine Geology 385 (2017) 160–172

Contents lists available at ScienceDirect

Marine Geology

journal homepage: www.elsevier.com/locate/margo

Bed-level changes on intertidal wetland in response to waves and tides: A case study from the Yangtze River Delta

Q. Zhu [a,b], B.C. van Prooijen [b], Z.B. Wang [a,b,c], S.L. Yang [a,*]

[a] State Key Laboratory of Estuarine and Coastal Research, East China Normal University, Shanghai 200062, China
[b] Department of Hydraulic Engineering, Faculty Civil Engineering and Geosciences, Delft University of Technology, P.O. Box 5048, 2600 GA Delft, The Netherlands
[c] Deltares, P.O. Box 177, 2600 MH Delft, The Netherlands

ARTICLE INFO

Article history:
Received 16 April 2016
Received in revised form 27 September 2016
Accepted 13 January 2017
Available online 18 January 2017

Keywords:
Intertidal wetland
Bed-level changes
Wind impact
Single-point model
Cyclicity of erosion and accretion
Yangtze River Estuary

ABSTRACT

Short-term bed-level variability in tidal wetlands has important implication both for ecology and engineering. In this study, we combined in situ measurements with model simulations to quantify short-term bed-level changes on a meso-macrotidal wetland in the Yangtze River Delta. On the middle flat, we observed erosion during neap-to-mean tides under onshore moderate-to-strong winds, and bed recovery during subsequent spring tides, when winds were both offshore and weaker, suggesting that winds can overturn the neap–spring cyclicity of bed-level changes even on meso–macrotidal mudflats. The magnitude of bed-level changes was smaller on both sides of the middle flat, while the smallest changes occurred on the salt marsh. Observed bed-level changes were reconstructed using a single-point bed-level change model, which incorporates in situ measured parameters of hydrodynamics (waves and currents), suspended sediment concentrations, and bed sediment properties. We conclude that the relative importance of waves and tides in intertidal wetland erosion and accretion can vary temporally (due to changes in balance between wave and tidal energies) and spatially (because of changes in elevation and vegetation in the cross-shore profile). Our study also reflects the advantage of combination of in situ measurement with simulation in detecting short-term variability of tidal flats.

1. Introduction

The morphological evolution of tidal mudflats has been extensively studied over recent decades, as healthy mudflats maintain vital ecological and environmental functions as well as protecting shorelines (Costanza et al., 1997; Goodwin et al., 2001; Barbier et al., 2008). Mudflats are sensitive to both natural and human-induced environmental changes. For example, previous research has shown that human activity, including land reclamation, shoreline protection, and the maintenance of navigation routes, in addition to upstream damming, can have a considerable impact on tidal flats (Yang et al., 2005; Chu et al., 2006; Blum and Roberts, 2009; Yang et al., 2011; Wang et al., 2015). In summarising human and climatic influences on meso-to-mega-scale morphodynamic developments, Wang et al. (2015) concluded that the quantitative determination of thresholds associated with regime shifts is vital to the sustainable management of tidal flats. Therefore, it is necessary to understand and predict the response of mudflats to disturbances by both natural and anthropogenic if we are to protect them against the future environmental changes.

However, quantifying the morphological response of tidal flats to human intervention remains challenging. Due to the often slow response times involved, it can be difficult to distinguish among the effects of various source of interference. In contrast, studies of short-term disturbance, such as storm events, are easier to validate and can provide valuable insights into the relationship between environmental changes and bed-level variability.

Numerous studies have sought to clarify the sedimentary processes that act on intertidal mudflats (see Mehta and McAnally (2008) and Friedrichs (2011) for recent overviews). Earlier work on the morphodynamic impacts of combined wave–current action on tidal flats suggests that waves, which are wind-related phenomena, are important agents of mudflat erosion (Green et al., 1997; Christie et al., 1999; Kim et al., 2000; Zhu et al., 2014). Many studies of wave effects on tidal flat morphology have focused on storm events (Ding et al., 2003; Fan et al., 2006; Palanques et al., 2006; Xu et al., 2015). Since moderate wave strength may also deeply affect sediment resuspension and transport (Green and Coco, 2014), study of normal wind effects on tidal flat bed-level variability is also needed. In addition, most studies have been based on either field measurements (Yang et al., 2003; Fan et al., 2006; Siadatmousavi and Jose, 2015) or numerical models (Ding et al., 2003; O'Shea and Murphy, 2013; Hu et al., 2015; Maan et al., 2015).

* Corresponding author.
E-mail address: slyang@sklec.ecnu.edu.cn (S.L. Yang).

http://dx.doi.org/10.1016/j.margeo.2017.01.003
0025-3227/

Studies combining field measurements and modelling are relatively scarce.

Detailed prediction strategies for bed-level changes over small spatial and temporal scales are still prone to considerable uncertainty. On the one hand, several key parameters can be difficult to quantify precisely. For example, the erodibility parameter, the erosion coefficient *M*, can vary by at least an order of magnitude (Whitehouse et al., 2000). Similarly, validation of erosion models can be limited by the techniques employed to measure bed-level changes at high temporal and vertical resolutions. Changes in bed level between each tidal submergences have been widely recorded (Kirby et al., 1992; Allen and Duffy, 1998; Bassoullet et al., 2000; O'Brien et al., 2000; Andersen, 2001; Yang et al., 2003; Andersen et al., 2006; Fan et al., 2006; Quaresma et al., 2007) and these studies provide valuable data to aid our understanding of the intertidal, neap–spring, seasonal, and longer-term evolution of mudflats surfaces. However, such data cannot elucidate the details of intratidal bed-level changes, which are key to understanding the mechanisms of bed evolution. With the development of self-logging instruments, high-resolution measurements of intratidal bed-level changes, together with sedimentary processes (currents, waves, and suspended sediment concentration), have become possible. Bed-level changes, for example, can be determined by repeated acoustic measurements of bed position (Gallagher et al., 1996; Jestin et al., 1998; Thornton et al., 1998; Christie et al., 1999; Saulter et al., 2003; Andersen et al., 2006; Andersen et al., 2007; Turner et al., 2008).

To improve the accuracy of prediction strategies for intertidal mudflats, we report here on the integration of data relating to wave and current regimes, suspended sediment concentrations (SSC), bed sediment properties, and observations of bed-level changes on an intertidal mudflat. The occurrence of strong winds during the measurement period allowed us to directly measure inter- and intratidal changes in bed level caused by wind events. We also describe a single-point BLC (bed-level change) model linking bed-level changes at high temporal and vertical resolutions with erosion and deposition fluxes, using in situ hydrodynamic and sediment property data. By validating the model using observational data, we attempt to: (1) calibrate the erosion coefficient *M* for the present study area; and (2) identify and quantify the main changes in the sedimentary processes during and after wind events. Our aim is to provide a greater insight into the sedimentary processes that operate at the bottom boundary layer of intertidal mudflats and their response to wind events.

2. Material and methods

2.1. Study site

We conducted in situ observations on an exposed tidal mudflat in the Eastern Chongming, which is located in the Yangtze River Delta, China (Fig. 1A). According to records from the Sheshan gauging station located 20 km east of our study site, the tides in the Yangtze Estuary are mixed semi-diurnal with an average range of 2.5 m, reaching up to 3.5–4.0 m during spring tides (Fig. 1A). Wind speed in this region is highly variable, with multi-year averages of 3.5–4.5 m/s and a maximum of 36 m/s (GSCI, 1988; Yang et al., 2008). Monsoon-driven winds are south-easterly during the summer and north-westerly in winter. Several storms hit the study area annually, with >10% of storms having wind speeds >25 m/s (Yang et al., 2003). Tropical cyclones impact the study area almost during every summer (Hu et al., 2007). Wind speed and direction data for 31.5°N 122.3°E were obtained from the European Centre for Medium-Range Forecasts (ECMWF) every 3 h over our study period.

The cross-shore bathymetry profile is shown in Fig. 1B, along with the position of our observation site. Our transect crossed the centre of a secondary channel, which was approximately 2 km in width and 8 m deep (Fig. 1). The cross-shore bathymetirc profile was convex-up, with the innermost 1.4 km being covered by salt marshes and the remainder being unvegetated mudflat. We measured bed-level changes at four sites along the cross-shore profile, corresponding to elevations of −1.21 m (Site 1: lower mudflat), 0.17 m (Site 2: middle mudflat), 0.52 m (Site 3: transition between mudflat and salt marsh) and 1.15 m (Site 4: salt marsh) above the mean sea level (Fig.1B). The dominant species of salt marsh vegetation at Site 4 is *Scirpus mariqueter*. The plant community of the salt marsh was measured to be 30 cm in crown height, 2 mm in stem diameter and 2000/m^2 in density. At Site 2, we conducted systematic measurements of wave, currents, SSC, bed level changes, and the properties of bed sediment.

Bed sediment on the mudflat generally consists of silt (median grain size <63 μm), >50% of which is coarse silt (32–64 μm; (Yang et al., 2008). When the tidal flat was exposed during the measurement periods, we observed only limited evidence of diatoms. In addition, bed ripple structures were not visibly affected by macro benthic species, which, judging by the low density of diatom holes, are relatively scarce at our site. Consequently, we consider the effects of such biological processes on our estimates of erosion and deposition rates to be minimal at this site.

2.2. Field experiments

2.2.1. Instrumentation

We used an Acoustic Doppler Velocimeter (ADV, 6.0 MHz Vector current meter, Nortek AS, Norway) to measure three-dimensional turbulent velocities in a 2.65 cm^3 volume of water. The ADV was fixed firmly to a tripod, with the transmitters oriented downwards and the emitter positioned 25 cm above the sediment surface. The sampled water volume, which was positioned 15.7 cm in front of the emitter, had a height of 9.3 cm. In addition, the ADV collected high-frequency pressure data that could be translated into water depth, wave heights, and wave periods. The measurement period was July 23 to August 3, 2011, during which time the ADV recorded 720 sets at a frequency of 8 Hz, resulting in a 1.5-minute sampling duration every 5 min.

Turbidity in the water column was measured every 5 min using optical back-scatter (OBS) sensors (OBS-3A, D&A Instrument Company, Washington, USA) attached to the tripod, with the probe positioned 15 cm above the sediment surface. Turbidity signals from the OBS sensors were converted into SSC values via calibration with in situ sediment samples. Regression between SSC and OBS-3A-derived turbidity yielded a correlation coefficient of 0.98 (Fig. 2).

2.2.2. Sampling and sediment analysis

Each day, we sampled surface sediment beneath the tripod during periods of daytime emergence. To avoid disturbing bed-level measurement area, we collected those samples at 2–3 m far away from the tripod center, where the ADV was located. Samples consisted of a mixture of at least four scrapes of the topmost 1–2 mm of bed sediment. The grain size distributions of each sample were analysed using a Coulter LS100Q laser diffraction particle size analyser (Beckman Coulter Inc., California, USA). Additionally, we collected mini sediment cores (10 cm long) during typical spring (July 26) and neap (August 2) tides to analyse the vertical distribution of erodibility. Each core was divided into three sections, with the top section being 2 cm long, and the lower two sections each 4 cm long. Except for grain size analysis, water contents of the mini cores were measured. Wet sediment samples were first weighed and then dried at 50 °C in an oven, before being reweighed for 48 h or more to obtain stable weights. We then derived the water content *W* from the ratio of water (the difference between wet and dry sediment weights) to dry sediment weights.

2.3. Bed-level measurements

Two methods were used to determine the bed level variations: the buried-plate method and the echo sounding function of the ADV. We used the former (Fig. 3) to measure relative bed-level changes between

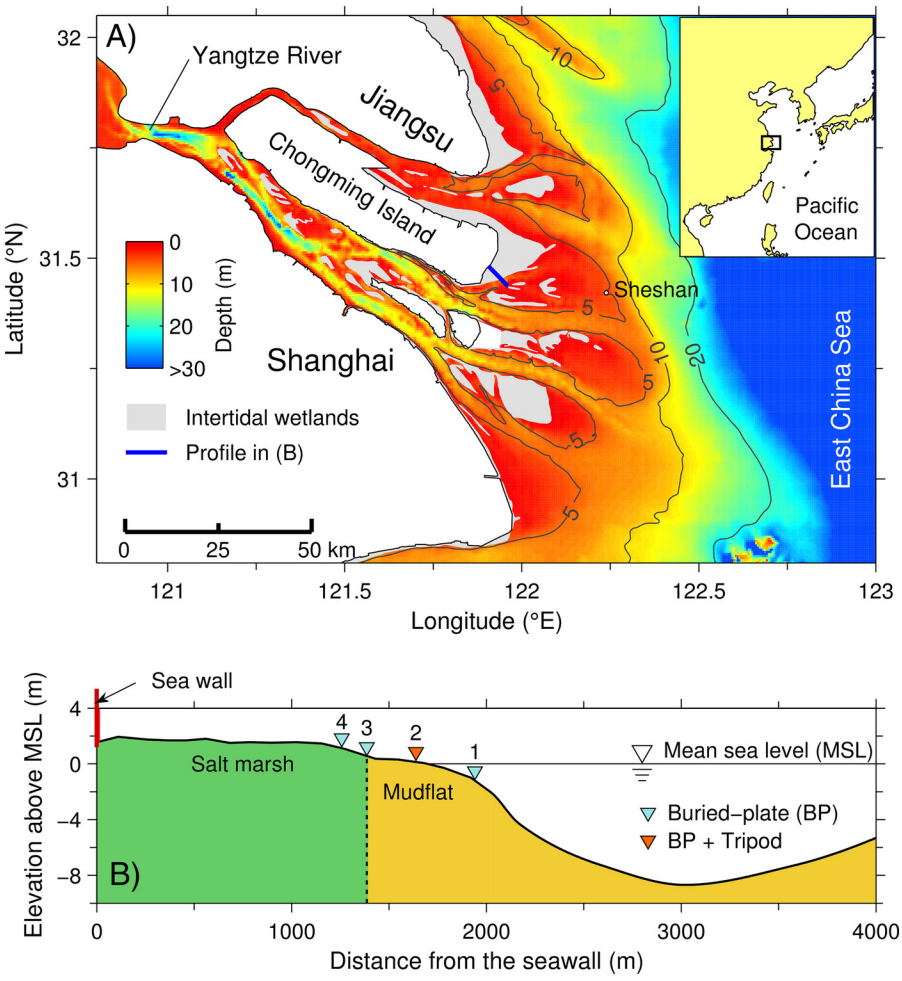

Fig. 1. (A) Map of the Yangtze River Delta showing the observation site; (B) cross-shore bathymetric profile on which the observation sites stand.

tidal cycles at the four sites. Specifically, a 25 × 25 cm ceramic tile was buried horizontally beneath the sediment surface, with a stick at each of the four corners to mark the plate's position. We then measured the distance between the sediment surface and the plate using 16 thin sticks inserted vertically into the sediment. The first data were recorded a day (two tidal cycles) after burial of the plate, by which time the flat had been restored to its undisturbed state. Relative bed-level changes were calculated from the difference between the two measurements. To minimize the signal from the ripples, we positioned eight sticks on ripple crests and a further eight within ripple troughs. The measured ripple height and length at Site 2 were 5.8 ± 1.3 mm and 59.7 ± 8.7 mm, respectively. At Site 2, we also used the second method to measure relative bed-levels, which recorded the distance between the ADV

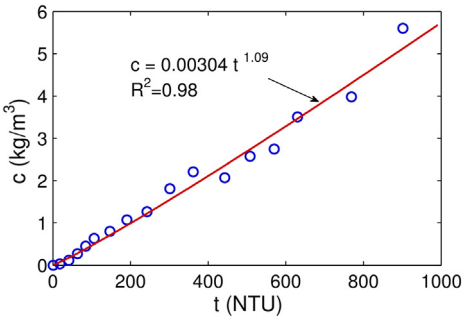

Fig. 2. Relationship between OBS-3A measured turbidity (t) and suspended sediment concentration (c).

transmitter and the sediment surface every 5 min, with an accuracy of ±1 mm (Andersen et al., 2006; Andersen et al., 2007; Shi et al., 2015).

2.4. Bed-level simulation

Changes in bed level are defined by the rates of erosion, E, and deposition, D, in kg/m^2/s:

$$\frac{\Delta\eta}{\Delta t} = \frac{1}{\rho_{dry}}(D-E) \tag{1}$$

where ρ_{dry} is the dry density of the bed sediment in kg/m^3. The variables used in the model are defined in Table 1.

Based on the stochastic nature of bed shear stress, van Prooijen and Winterwerp (2010) proposed an erosion-rate formula in which the third-order polynomial fit is expressed as in Eq. (2). Although this formula is derived for flow only, we extended its application to combined wave–current conditions, which is similar to the treatment of the Ariathurai-Partheniades equation (Partheniades, 1965; Ariathurai, 1974):

$$E = M\tau_e \begin{cases} 0 & ,\frac{\tau_{cw}}{\tau_e}\in[0,0.52) \\ a_1\left(\frac{\tau_{cw}}{\tau_e}\right)^3 + a_2\left(\frac{\tau_{cw}}{\tau_e}\right)^2 + a_3\left(\frac{\tau_{cw}}{\tau_e}\right) + a_4 & ,\frac{\tau_{cw}}{\tau_e}\in[0.52,1.7] \\ \left(\frac{\tau_{cw}}{\tau_e}-1\right) & ,\frac{\tau_{cw}}{\tau_e}\in(1.7,+\infty) \end{cases} \tag{2}$$

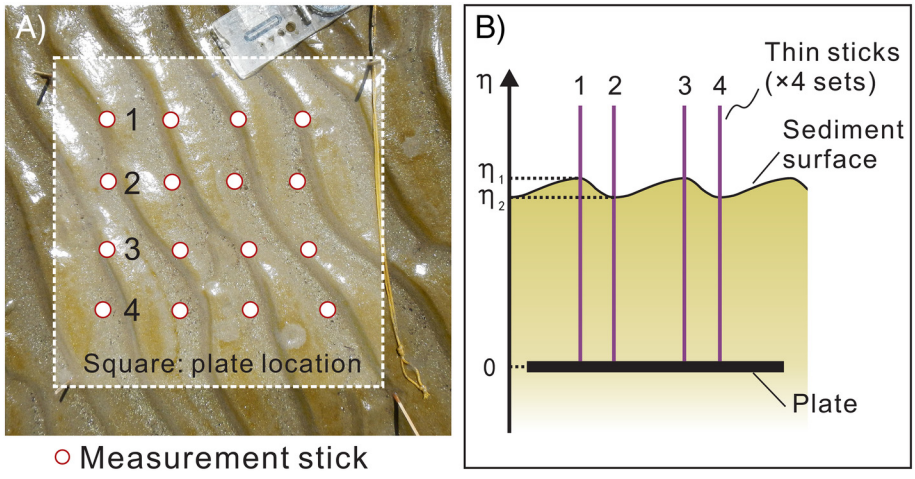

Fig. 3. Buried-plate method measures relative bed level change. (A) is the plane view of a real sediment bed showing sticks assignment; transactional view (B) shows sticks are located evenly at ripple crests and troughs.

in which the constants $a_1 = -0.144$, $a_2 = 0.904$, $a_3 = -0.823$, and $a_4 = 0.204$; M (s/m) is the erosion rate coefficient, and τ_{cw} (Pa) is the total bed shear stress due to the combined effects of wave and current action, calculated as shown in the Appendix. The variable τ_e (Pa) is the critical bed shear stress for erosion calculated as (Taki, 2001):

$$\tau_e = 0.05 + \beta\left\{\left[\frac{\pi}{6}(1+sW)\right]^{\frac{1}{3}} - 1\right\}^{-2} \tag{3}$$

where W is the measured water content (see Section 2.2.2) and $s = \rho_s/\rho_w - 1$ is the submerged specific weight of bed sediment, in which ρ_s and ρ_w are the measured densities of sediments (2560 kg/m^3) and seawater (1012 kg/m^3), respectively. The coefficient β ranges from 0.1 to 2.0, and in the present study we used $\beta = 1.0$.

The deposition rate, D, in Eq. (1) is derived from the sediment flux at the bed according to the following two deposition modes:

$$D = c_b\omega_s \tag{4}$$

or

$$D = \begin{cases} 0 & , \tau_{cw} > \tau_d \\ c_b\omega_s, & \tau_{cw} \le \tau_d \end{cases} \tag{5}$$

where c_b (kg/m^3) is the near-bed SSC measured by the OBS-3A, ω_s (m/s) is the settling velocity of suspended sediment, and τ_d (Pa) is the critical bed shear stress for deposition. In our study, effort is made on the simulations shown in Table 2.

Table 1
Selected notations in the single-point bed level change (BLC) model.

Notation	Variable name	Illustration
η	Bed level	Simulated/measured
ρ_{dry}	Dry density	$f(W)$
W	Water content	Measured from sediment cores
E	Erosion rate	Simulated, $f(\tau_{cw}, \tau_e, M)$
τ_{cw}	Total bed shear stress under combined wave–current action	Simulated using in situ measured hydrodynamic parameters
τ_e	Critical bed shear stress for erosion	$f(W)$
M	Erosion coefficient	Calibrated from the model
D	Deposition rate	Simulated, $f(\omega_s, c_b, \tau_d)$
ω_s	Settling velocity	Simulated, $f(c_b)$
c_b	Near-bed suspended sediment concentration	In situ measured
τ_d	Critical bed shear stress for deposition	$=0.5\tau_e$

The group settling velocity of cohesive sediment, ω_s (m/s), is strongly dependent on the SSC and can be estimated as:

$$\omega_s = E_1 c_b^{E_2} \tag{6}$$

in which E_1 and E_2 are constants that vary among estuaries (Whitehouse et al., 2000). In the present study, E_1 and E_2 were set to 0.002 and 1.5, respectively, for Eqs. (6) and (7).

Increased sediment concentration over a certain limit results in decreased settling velocity, which is described as hindered settling. This process must be accounted for when estimating deposition fluxes in shallow water, as layers of high sediment concentration are common in estuaries and bays, as well as on continental shelves and intertidal flats (Kineke et al., 1996; Traykovski et al., 2000; McAnally et al., 2007; Zhu et al., 2014). To determine ω_s while also considering hindered settling, we followed the formula of Whitehouse et al. (2000). The effective diameter, d_e, of a floc increases with the volume concentration $C = c_b/\rho_s$ via the following relationship:

$$d_e = lC^{\frac{E_2}{2}} \tag{7}$$

where the length-scale l is given by:

$$l = \left[\frac{19.8\rho_w\nu\rho_s^{E_2}E_1}{g(\rho_e - \rho_w)}\right]^{0.5} \tag{8}$$

in which constants E_1 and E_2 are the same as in Eq. (6), ν is the kinematic viscosity of water, g is gravitational acceleration, ρ_w and ρ_s are the densities of water and sediment, respectively, and $\rho_e = \rho_w + 0.03(\rho_s - \rho_w)$ is the effective density of the floc. The volume concentration of flocs is given as:

$$C_f = \frac{(\rho_s - \rho_w)C}{\rho_e - \rho_w} \tag{9}$$

Therefore, settling velocity ω_s can be expressed as:

$$\omega_s = \frac{d_e}{\nu}\left\{\left[10.36^2 + 1.049(1-C_f)^{4.7}D_*^3\right]^{0.5} - 10.36\right\} \tag{10}$$

Table 2
Simulation codes with different conditions.

Run ID	Erosion				Deposition		Recovery stage (RS) modification				
	M (s/m)	W (%)	τ_e (Pa)	ρ_{dry} (kg/m^3)	Model	τ_d (Pa)	M (s/m)	W (%)	τ_e (Pa)	ρ_{dry} (kg/m^3)	τ_d (Pa)
1	0.0019	32	0.29	1414	Eq. (4)	/	Off				
2	0.0014	32	0.29	1414	Eq. (5)	0.15	Off				
3	0.0014	32	0.29	1414	Eq. (5)	0.15	0.00056	98	0.14	736	0.07
4	0.0014(1 ± 50%)	32	0.29	1414	Eq. (5)	0.15	0.00056 (1 ± 50%)	98	0.14	736	0.07

where D_* is the dimensionless floc diameter given by:

$$D_* = d_e\left[\frac{g(\rho_e-\rho_w)}{\rho_w\nu^2}\right]^{\frac{1}{3}} \quad (11)$$

3. Results

3.1. Wind conditions

Wind direction was variable during our field campaign. Prior to July 31 and after August 2, the prevailing wind direction was onshore (Fig. 4A) and wind speed was generally moderate (6.8 ± 2.1 m/s). The maximum onshore wind velocity (11 m/s) occurred on July 27. A weak (2.6 ± 1.1 m/s) offshore wind flow characterised the period July 31–August 2.

3.2. Hydrodynamic conditions and bed shear stresses

The tides changed from neaps to springs during the measurement period. A maximum water depth of 2.2 m occurred during tidal cycle 14 (Fig. 4B). ADV-derived mean near-bed current velocities ranged from 0.004 to 0.5 m/s, with an average value of 0.18 m/s (Table 3). The average significant wave height was 0.25 m and 0.11 m during the windy and calm periods, respectively.

The total bed shear stress due to the combined effects of wave and current action, τ_{cw}, ranged from 0.007 to 2.97 Pa, with an average value of 0.81 Pa for the measurement period. Values of τ_{cw} were lower during periods of diminished wind speed. Increase in τ_{cw} during windy periods is due to the wind generated enhancement of τ_w and wind-induced extra turbulence influencing τ_c (Zhu et al., 2016).

3.3. Suspended sediment concentrations

Because near-bed SSC, c_b, varies over the course of a tidal cycle, to reduce complexity, we plotted the tide-averaged value (Fig. 4D). The average for tidal cycles 1–13 was $c_b = 0.4$ kg/m^3 (Fig. 4D), but increased to 1.7 kg/m^3 after cycle 14. We stress that the increase in SSC cannot be due to contamination of the OBS optical probe because the probe was cleaned daily with fresh water. The offshore surface SSC at Sheshan (see Fig. 1A) shows a similar pattern to our study site (Fig. 4D),

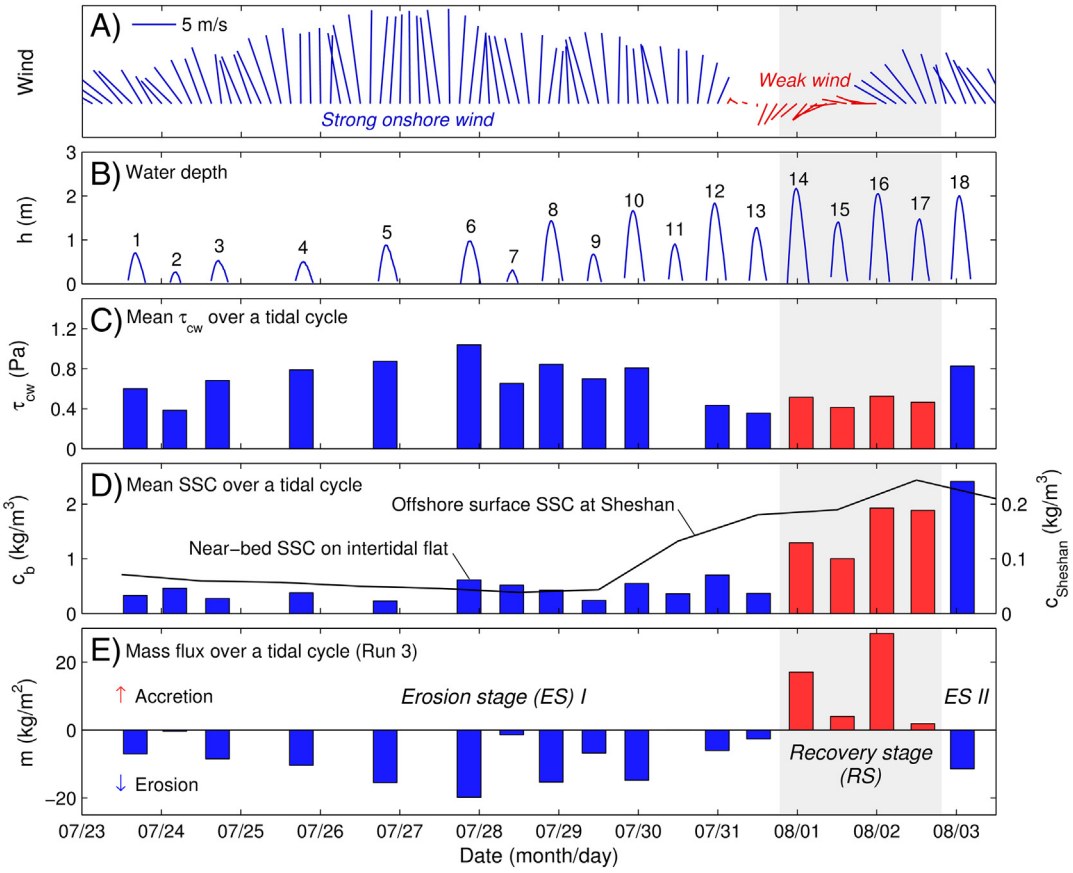

Fig. 4. Time series of (A) wind vectors, (B) water depth (h), (C) tide-average value of combined wave–current bed shear stress (τ_{cw}), (D) tide-average near bed suspended sediment concentration (SSC, c_b) observed by OBS-3A, and surface SSC obtained at Sheshan ($c_{Sheshan}$, see Fig. 1B), and (E) vertical sediment flux over each tidal cycle.

Table 3
Descriptive statistics for velocity speed (U_c), significant wave height (H_s), and bed shear stresses (τ_w, τ_c, τ_{cw}).

BSS	Erosion stage			Recovery stage			Full period		
	Ave.	Max.	Min.	Ave.	Max.	Min.	Ave.	Max.	Min.
U_c (m/s)	0.17	0.51	0.004	0.19	0.41	0.02	0.18	0.51	0.004
H_s (m)	0.24	0.46	0.07	0.14	0.30	0.08	0.21	0.46	0.07
τ_w (Pa)	0.28	0.68	0.01	0.07	0.47	0.01	0.22	0.68	0.01
τ_c (Pa)	0.55	2.43	0.03	0.43	1.97	0.01	0.51	2.43	0.01
τ_{cw} (Pa)	0.72	2.47	0.07	0.48	1.99	0.03	0.66	2.47	0.03

indicating that SSC increased on a regional scale towards the end of the first onshore wind stage.

3.4. Bed properties

The critical bed shear stress for erosion, τ_e, was calculated as 0.29 Pa using Eq. (3) and a constant water content of 32%. The average median grain size of surficial sediment during the first onshore wind stage was 65 μm, with a mud (<62.5 μm) content of 46% (Fig. 5). On August 1, during the period of weak offshore wind, median grain size decreased to 26 μm and the mud content rose to 100%.

3.5. Measured bed-level changes

Both the ADV and buried-plate measurements at the site 2 recorded bed degradation during strong wind conditions (tidal cycles 1–13) and bed accretion when the wind dropped and became offshore (tidal cycles 14–17; Fig. 6A). We refer to these discrete periods of degradation and accretion as erosion stages (ES I; 1–13, and ES II; 18) and recovery stages (RS; 14–17), respectively, based on the behaviour of the bed level.

The ADV measurements showed that the bed level differs between the beginning and end of inundation periods (Fig. 6A), indicating that bed-level variability occurs even in water depths <0.25 m. It indicated that hydrodynamic forces still act on the bed during very shallow waters. Dewatering process was considered to contribute to the bed-level variability in these stages when the bed position at beginning of a tidal inundation period was lower than that at the end of the previous tidal inundation period. However, because this process cannot be detected by direct measurement or modelling, we modified the ADV-measured bed levels by subtracting the intertidal difference in bed position for comparison with simulated values.

During the transition from the erosion to the recovery stage, we observed differences in the magnitude of bed-level change between the ADV and buried-plate derived measurements. The maximum erosion depths obtained by the buried-plate and ADV approaches were 6.9 and 10.6 cm, respectively, and occurred after tidal cycles 13 and 12, respectively (Fig. 6A). These differences were most probably caused by the slight difference in the positions at which the two techniques were used, the plate being buried approximately 5 m from the ADV. Additionally, the ADV measurements were affected by scouring around the frame.

Overall, bed-level changes on the mudflat were greater than on the salt marsh, with maximum values observed on the middle flat (Site 2). During the first erosion stage, cumulative erosion at Site 2 reached ~3 cm, whereas bed-level changes at the other sites were less than ±0.5 cm. During the recovery stage, all four sites experienced accretion, with maximum values at Site 2 and minimum values at Site 4 (salt marsh). During the second erosion stage, erosion was greatest at Site 2, followed by Site 1 (low flat) and Site 3 (transition between flat and marsh) with almost no erosion occurring at the marsh site (Fig. 6C).

3.6. Simulated bed-levels

Bed level can be calculated using Eq. (1) by incorporating velocity, wave, and sediment concentration measurements. Using the constant M and τ_e, we simulated bed-level changes during the ES I (Fig. 6B, Runs 1 and 2). From tidal cycle 14 onwards, the accretion in Run 1 was considerably faster than the measured accretion. By the end of the simulation period, the relative bed level increases by as much as 40 cm, which is far greater than the observed values. For Run 2, we applied a deposition threshold of $\tau_d = 0.14$ Pa, with the result that the excessive accretion no longer occurred. We also note that the simulated bed-level series for each tidal cycle are smoother than those measured by the ADV, indicating that ADV-derived intratidal bed levels exhibited greater variability than the simulated bed levels (Fig. 7D_1).

4. Discussion

4.1. Differences between measured and simulated changes in bed level

The observed fluctuations in the measured bed level (Fig. 7D_1) may have been caused partly by measurement errors. For example, the ADV records bed-level changes every 5 min. In most burst intervals, bed-level variations ranged from 0 to 10 mm, with the majority (96%) ranging from 0 to 5 mm. This rate of variability is similar to the accuracy (1 mm) of the ADV sensor used for bed-level measurement. By incorporating a moving average, this noise can be minimised. However, such smoothed bed-level series obtained from the ADV exhibit a periodic signal, which is absent in our simulations, and we hypothesise that this disparity is related to the migration of bed ripples. The magnitude of this fluctuation (10–13 mm) is indicative of the bed ripple height, H_r. Manual measurements show that H_r varied from 3 to 20 mm and L_r varied from 28 to 107 mm (Table 4). Our values agree with those of Baas et al. (2013), who reported that H_r values in their flume-based experiments using sand-mud mixture were of the order of millimetres, with ripple lengths L_r measured in centimetres.

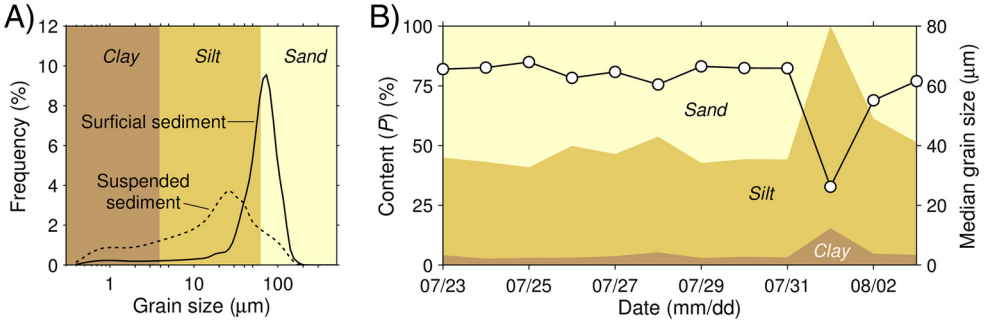

Fig. 5. (A) Grain size distribution of surficial sediment sampled below the tripod and instantaneous suspended sediment sampled manually. Each line is the mean frequency curve of 12 surface bed samples and 4 suspended sediment samples, respectively. (B) Time series of clay, silt and sand components and median size of surficial sediment.

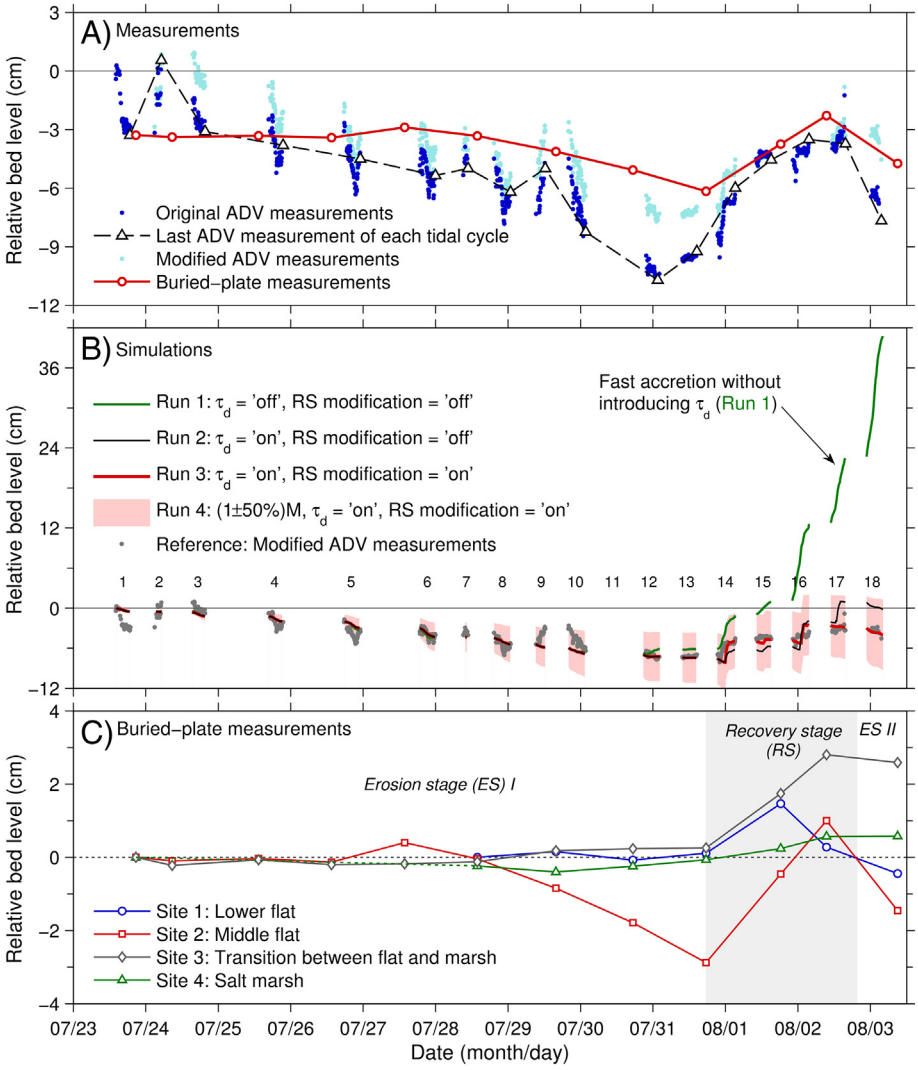

Fig. 6. Time series of (A) measured, (B) simulated bed level changes, and (C) buried-plate measurements. To compare with simulated bed level later, ADV measurements are modified with removal the bed level difference between each two measured tidal cycles. 'RS modification' in (B) indicates if erosion parameter *M* and *W* are modified in the recovery stage.

The ratio of ripple length to periodicity reflects the ripple migration rate V_r (Table 4). Lin and Venditti (2013) derived an empirical relationship between V_r and other physical parameters:

$$\frac{V_r}{\omega_s} = 0.00127\left(\frac{\theta}{\theta_e}\right)^{0.989} \times BCF \tag{12}$$

in which ω_s is the settling velocity of the sediment concentration near the bed, $\theta = \tau_{cw}/[(\rho_s-\rho_w)gD_{50}]$ and $\theta_e = \tau_e/[(\rho_s-\rho_w)gD_{50}]$ are the Shields number and critical Shields number, respectively, for sediment entrainment, and *BCF* is a bias correction factor dependent on the ratio of water depth to sediment grain size, h/D_{50}. *BCF* was determined after Lin and Venditti (2013). In our study, the calculated rate of ripple migration was approximately 10^{-5} m/s, which aligns with the estimates based on the ADV-monitored bed level and measured ripple length (Table 4). We note the difference in magnitude is caused partly by the uncertainty associated with the ripple length. As manual measurements of ripple length are temporally sparse, $L_{r,meas.}/T_{r,ADV}$ is estimated from the closest measurement of $L_{r,meas.}$.

Several arguments have been raised concerning critical bed-shear stress during deposition, τ_d. Although some have argued that erosion and deposition occur simultaneously (Winterwerp, 2007), other studies of sediment dynamics have incorporated τ_d into their assessments (Krone, 1962; Dyer, 1986; Christie et al., 1999; Lumborg, 2005). As shown in Fig. 6B, our results support the model of deposition occurring when total bed shear stress is smaller than τ_d. However, it is also likely that sediment particles settle because of gravity. Here, we define the falling motion of sediment as 'settling' and the product as 'deposition': sediment is always settling under the influence of gravity, whereas deposition is not constant. For example, if bed shear stress is insufficiently low to allow deposition, sediment can remain in suspension in the near-bed water column, resulting in no change in bed level.

This scenario, which is incorporated into Eq. (5), supports the model of bed degradation during the second erosion stage (ES II). Table 5 shows that the magnitude of erosion parameters (τ_{cw}, τ_e, and M) in the two erosion stages is similar, whereas deposition parameters c_b and ω_s are 6 and 9.2 times larger, respectively, in ES II than in ES I. Were the deposition rate not controlled by τ_d (i.e., constant deposition), bed level would increase considerably and degradation would not occur during the second erosion stage.

4.2. The effect of strong winds on bed-level

In contrast to storm conditions (wind speed > 10.8 m/s), the morphological effects of strong wind conditions (wind speed < 10.8 m/s) on meso- to macrotidal flats have not received much attention. Fig. 6A_1–A_2 shows that the near-bed current speed varies with tidal range. Without the effect of waves, variations in current speed result

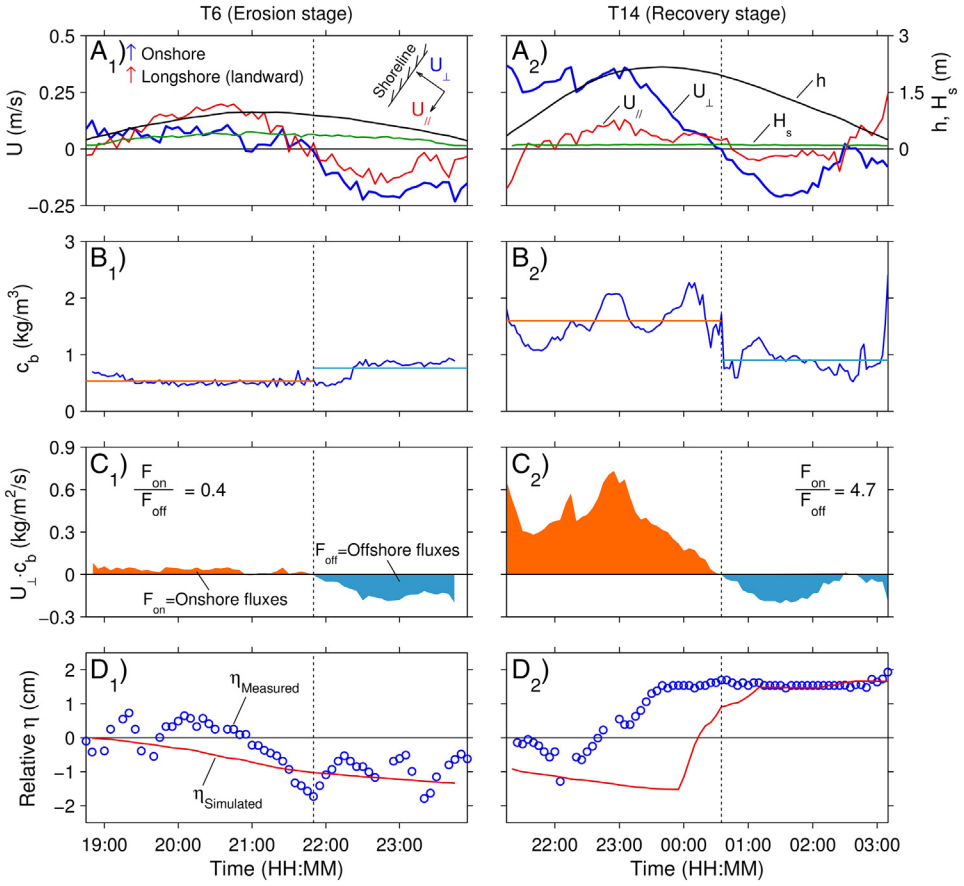

Fig. 7. Time series of intra-tidal (A) onshore ($U_{\perp}$) and longshore velocities ($U_{\parallel}$), with water depth (h) and significant wave height (H_s), (B) Near-bed suspended sediment concentration (c_b), (C) Cross-shore near-bed sediment fluxes, and (D) ADV monitored (circle) and simulated (red line) relative bed level (η) in a typical erosion tidal cycle (T6) and a typical recovery tidal cycle (T14). (For interpretation of the references to colour in this figure legend, the reader is referred to the web version of this article.)

in bed-level changes. Yang (1991) concluded that when wave forces exceed tidal forces, tidal cyclicity in bed-level changes is curtailed by waves. In our study, the mean wind speed during the measurement period was close to the year-averaged value, demonstrating that even normal wind conditions can modify the neap–spring cyclicity of bed-level changes. Total bed shear stresses are higher over windy neap tides than during calm spring tides (Fig. 4C). We note, however, that sediment concentrations are higher during spring tides than neap tides, a pattern that implies channel concentrations are following the spring–neap cycle.

Additionally, wind also serves to break the intratidal cyclicity of bed-level changes. On middle flats, tidal inundation begins with the peak flood flow, is characterised by slack water at high tide, and concludes with the peak ebb flow. According to Whitehouse et al. (2000), the bed alternates between degradation and accretion over the course of these three stages. In the present study, however, τ_{cw} values during over 90% of erosion stage were higher than the critical bed shear stress for erosion τ_e, indicating that erosion is a constant process whereas accumulation is comparatively rare. This imbalance results in net erosion of the bed during tidal inundation (Fig. 7D$_1$).

The impacts of wind events on coastal bed-level change varies spatially and temporally. In terms of sediment balance, erosion at one area must correspond to accretion at another. For example, during a storm event when erosion was documented on a mudflat, accretion was observed in the adjacent salt marsh and subtidal channel (Yang et al., 2003; Andersen et al., 2006). In general, the magnitudes of erosion and accretion on mudflats are larger than on salt marshes, since salt marsh vegetation dissipates the wave energy and weakens the wave

Table 4
Results of bed ripple size (height, H_r, and length, L_r), period (T_r) and migration rate (V_r). Simulated ripple migration rate is tidally averaged.

Tidal cycle ID	Ripple height				Ripple length		Period		Ripple migration rate V_r ($\times 10^{-5}$ m/s)	
	Manually meas.		ADV monitored		Manually meas.		ADV monitored			
	H_r (mm)	N	H_r (mm)	N	L_r (mm)	N	T_r (s)	N	$L_{r,meas}/T_{r,ADV}$	Simulated
3	–	–	5.4 ± 1.3	5	–	–	4258 ± 483	4	1.1	1.2
5	5.9 ± 1.6	20	5.0 ± 0.4	3	47.9 ± 5.6	20	–	–	–	1.1
6	–	–	7.9 ± 2.1	6	–	–	2926 ± 284	6	1.6	5.3
8	–	–	3.4 ± 1.3	6	–	–	2050 ± 326	3	2.3	2.7
9	–	–	–	–	43.0 ± 8.5	24	–	–	–	–
10	–	–	11.8 ± 1.6	5	–	–	3692 ± 1129	6	1.3	3.7
11	–	–	3.9 ± 1.2	3	59.2 ± 7.1	48	–	–	–	2.9
12	12.6 ± 3.2	16	1.6 ± 0.4	4	86.5 ± 12.7	36	3719 ± 965	2	2.3	0.6

Table 5
Values of selected parameters in three stages.

	Erosion process			Deposition process	
	M (s/m)	τ_e (Pa)	τ_{cw} (Pa)	c_b (kg/m^3)	ω_s (mm/s)
Erosion stage I	0.0014	0.29	0.71 ± 0.36	0.4 ± 0.2	0.6 ± 0.3
Recovery stage	0.00056	0.14	0.48 ± 0.42	1.5 ± 0.6	3.2 ± 1.5
Erosion stage II	0.0014	0.29	0.83 ± 0.40	2.4 ± 0.5	5.5 ± 1.2

action on bed sediments (Yang et al., 2012). Even on a mudflat itself, the magnitude of erosion and accretion during a wind event can vary with elevation (Fan et al., 2006).

4.3. Bed recovery

Previous studies have shown that bed accumulation on intertidal wetlands follows wind-induced erosion (Pejrup, 1988; Yang et al., 2003; Andersen et al., 2006; Friedrichs, 2011). In our study, this recovery was rapid. After an eight-day period of erosion, for instance, the bed had nearly recovered its original position within two days. Sediment supply plays a fundamental role in bed recovery. The similar pattern of SSC variability between intertidal and subtidal flats (Fig. 4D) suggests that there was an injection of sediment into both zones during the recovery stage. Pejrup (1988) demonstrated that onshore sediment fluxes are favourable under tide-dominated conditions. Sediment for bed recovery might also be supplied by the Yangtze River (Yang et al., 2003).

The increase in SSC and rapid bed recovery both occurred following tidal cycle 14, which marked the onset of a period of low wind speeds (Fig. 6), rather than after tidal cycle 13. This is because the tidal range of cycle 14 exceeded that of cycle 13, resulting in a greater availability of tidal energy to erode and transport sediment from deeper waters. Additionally, we infer that the recovery stage coincided with the spring tide, which served to promote bed recovery.

The process of bed accretion occurs primarily through the settling-lag and scour-lag (Van Straaten and Kuenen, 1958; Postma, 1961; Pejrup, 1988) associated with tidal asymmetry (Friedrichs, 2011). In Fig. 7A$_2$–C$_2$, which shows the intratidal velocities, sediment concentration and near-bed sediment fluxes during a typical recovery tidal cycle, c_b was higher during the flood stage than the ebb stage. This pattern is the reverse of c_b variability during the erosion stage (Fig. 7B) and dominates the net onshore transport of sediment. Tidal asymmetry (Fig. 7A$_2$) during the flood stage also serves to enhance net onshore sediment transport (Fig. 7C$_2$). If sufficient distribution data are available, a detailed model of net sediment transport along a cross-shore transect can be derived from the analysis of grain size trends (Wang et al., 2012). On the one hand, enhanced high-energy flood flow will increase the bed shear stress, potentially resulting in bed erosion. However, as indicated by the layered bed model, deeper beds exhibit greater shear strength (Zhou et al., 2016), which, together with a decrease in τ_{cw} (Fig. 4C), limits the magnitude of erosion. On the other hand, high-energy flood flow can transport considerable volumes of sediment onshore, whereas lower-energy ebb flow will remove comparatively less sediment offshore.

The settling time is also important to net bed accretion. In our study, sediment settling occurs 30% of measured tidal submergence in recovery stage by taking $\tau_d = 0.14$ Pa. Pejrup (1988) noted that the settling-lag and scour-lag processes are only effective during periods of high SSC (Fig. 7B$_2$) when stimulated flocculation produces large settling velocities that serve to enhance deposition at slack water.

In summary, recovery is rapid when: (1) abundant sediment is delivered by high-energy tidal flows, probably during spring tides; (2) tidal asymmetry favours flood dominance, leading to greater onshore sediment transport; (3) τ_d exceeds τ_{cw} long enough to promote sediment deposition; and (4) high SSC enhances flocculation, which also promotes settlement.

Fig. 8 depicts the key processes operating in the three stages (ES I, RS, and ES II). The ADV-derived bed-level time series (Fig. 6) shows rapid bed accretion during tidal cycle 14. Concurrently, the mud content increased from 50% in the erosion stage to 100% during the recovery stage (Fig. 5B). We suggest that the original coarser-grained bed became covered by a fresher, finer-grained layer. Such a change in bed condition undoubtedly affects the erodibility parameters M and τ_e in the recovery stage (Fig. 8B). Water content W dictates τ_e according to Eq. (3), and also serves to influence ρ_{dry} (Eq. (1)).

4.4. Application of the model to variations in erosion parameters

In a recent study of hurricane-induced sediment transport on the Louisiana shelf, Xu et al. (2015) concluded that near-bed sediment fluxes are sensitive to model parameters. The erosion coefficient M, one of the key parameters in the Eq. (2) erosion model, is typically obtained by extensive laboratory testing (Whitehouse et al., 2000). In this study, we propose an approach to calibrating M that uses in situ measurements. Specifically, we introduced the index of agreement I (Willmott et al., 1985) to compare bed-level series simulated using different M to ADV measurements:

$$I = 1 - \frac{\sum (x-y)^2}{\sum \left(|x-\bar{y}| + |y-\bar{y}|\right)^2} \tag{13}$$

where x and y are the two datasets being compared. Values for I range from 0 to 1, with $I = 0$ indicating no agreement and $I = 1$ indicating perfect agreement. The best estimation of M corresponds to the highest value for I.

Our analysis of the mini-core samples revealed that the sediment water content, W, was stable in the upper 10 cm but decreased slightly from 32% to 30% with depth down core. This pattern indicates that the erosion coefficients M and τ_e might be considered constants during ES I. Based on this assumption, we calculated M as 0.0014 s/m (Fig. 9).

A systematic means for calculating M, presented by Winterwerp and van Kesteren (2004), requires several key soil mechanical parameters. In the present study, however, data pertaining to the recovery stage W and sediment water content were unavailable. Consequently, we conducted a model-based test to evaluate the degree to which M and W (τ_e and ρ_{dry}) vary during the recovery stage. Our most recent sediment sample from the bed surface indicates that the bed-sediment component during the final cycle was similar to that of the ES I (Fig. 5B). Measurements of water content exhibit a similar pattern. Therefore, we consider that the bed sediment properties during the last tidal cycle were similar to those of the first erosional stage, with the result that M and W modifications need to be applied only to tidal cycles 13–17.

Fig. 10A shows that to obtain bed levels that are in close agreement with our measurements, M decreases from 0.0014 s/m to 0.00056 s/m during the erosion stage, while W increases from 32% to 98%. The increase in W is responsible for the decrease in τ_e, as a high water content results in a looser particle structure and more erodible sediment. During the recovery stage, τ_e becomes 0.14 Pa, which is consistent with the findings of Whitehouse et al. (2000) that τ_e for recently deposited mud is only 0.1–0.2 Pa. Sediment mass fluxes are also lower (Fig. 10B), leading to improved simulations of bed level (Fig. 6B, Run 2 vs. Run 3).

In practice, we consider M to be constant within a certain period when bed properties do not change significantly. Typical values for $M \cdot \tau_e$ vary from 10^{-5} to 5×10^{-4} kg/m^2/s (Winterwerp and van Kesteren, 2004). In our study, values for $M \cdot \tau_e$ were 4.1×10^{-4} kg/m^2/s and 7.8×10^{-5} kg/m^2/s during the erosion and recovery stages, respectively. We note that although M and W both changed over the course of the experiment, it is plausible that these changes are related. For example, M is determined in part by the dry density and volume concentration of bed sediment, both of which are related to W (Winterwerp and van Kesteren, 2004).

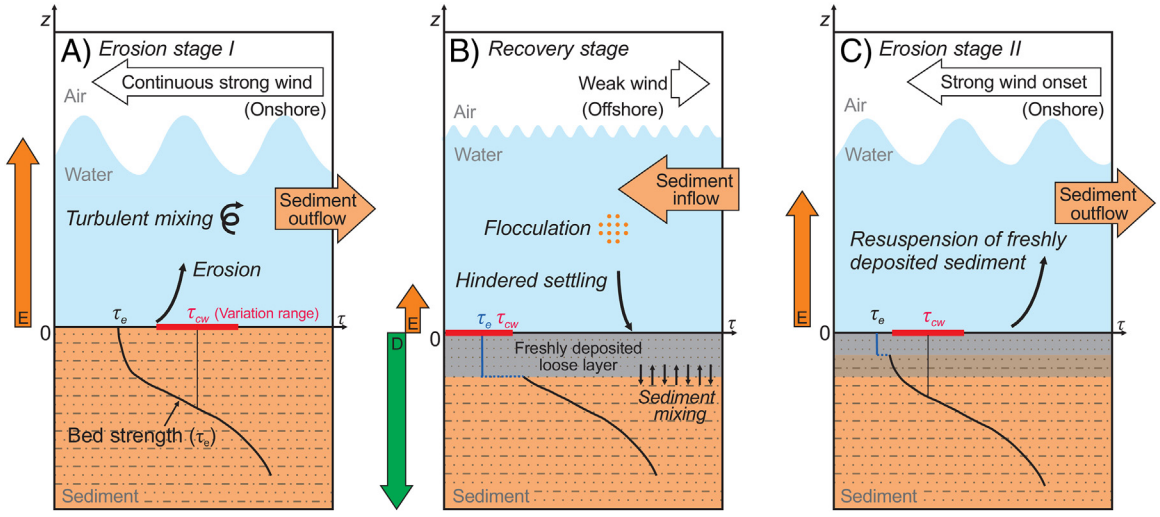

Fig. 8. Schematic diagrams inllustrate the key processes in three stages. Original vertical distribution of bed strength, representing τ_e, is redrawn after Winterwerp et al. (2012).

The strength of surface mud layers may also be weakened by liquefaction, which is a direct result of enhanced wave strength during storms and hurricanes (Teisson et al., 1993; van Kessel and Kranenburg, 1998; Jaramillo et al., 2009). Laboratory studies showed that liquefaction occurs when wave-induced stress within the bed exceeds the bed's yield strength. During liquefaction, a fluid mud layer can develop, which is derived from the surface sediment layer (van Kessel and Kranenburg, 1998). This processes serves to augment high transport rates during wind events. Liquefaction induced increase in water content of bed sediment may decrease the bed erodibility, and directly affect the bed level by changing bulk density. Although we observed no evidence of liquefaction (i.e., increase in near-bed SSC; Fig. 4D), and thus did not include the effect in our model, we stress that it is important to estimate sediment fluxes in the studies of mud-rich areas under conditions of high wave energy.

4.5. Limitations of the model

The erosion process described in Eq. (2) refers to surface erosion only. In reality, however, there are four erosion modes for cohesive sediment (Winterwerp and van Kesteren (2004): entrainment of mud layers, floc erosion, surface erosion, and mass erosion. When bed shear stress exceeds a certain threshold (i.e., the remoulded bed strength), local failure occurs within the bed, resulting in the formation of cracks. This type of erosion is often observed as sheet erosion on intertidal flats (Fig. 11). Although sheet erosion did not occur immediately adjacent the observation frame, we did observe it in the vicinity of the measurement site and throughout the lower intertidal flat. This mass erosion process proved to be crucial to estimates of total sediment transport in and out of the tidal flat system, as mass erosion typically occurs during wave attack (Winterwerp and van Kesteren, 2004).

Sediment reworking has commonly been reported for tidal flats on different temporal scales (Andersen and Pejrup, 2001; Maire et al., 2008; Webster et al., 2013). ON the basis of isotope dating, and bed-level measurements made over more than three years, Andersen and

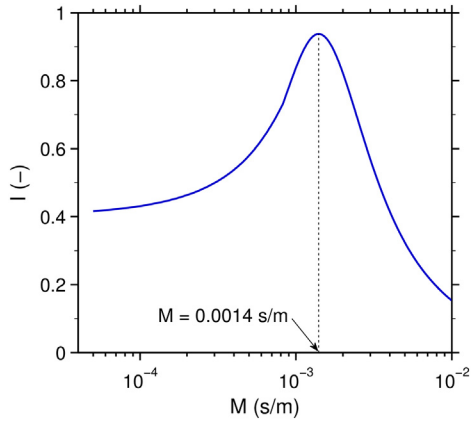

Fig. 9. Diagram showing erosion coefficient M in Eq. (2) determining the accordance, indicated by index of agreement I, of simulated bed level with ADV measurements. $M = 0.0014$ s/m provides the best estimation in the first erosion stage.

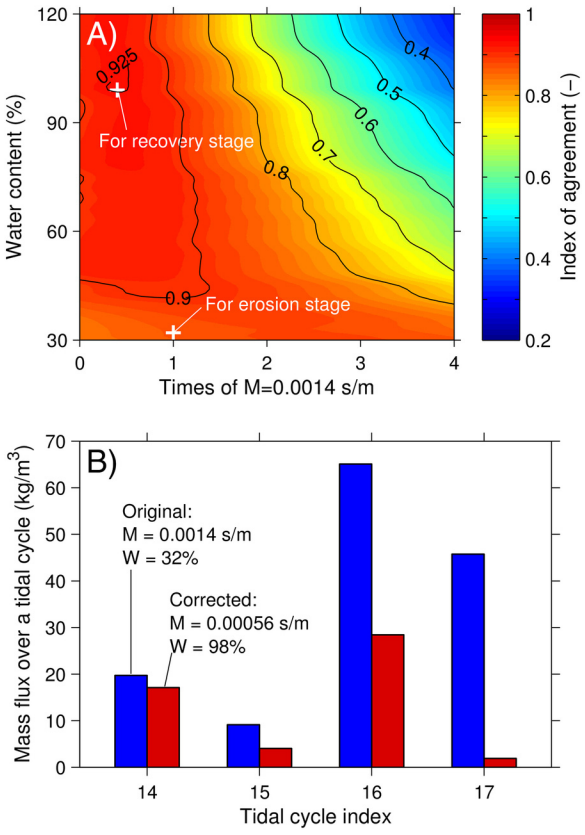

Fig. 10. (A) Calibration of erosional parameters M and W for recovery stage. It provides best bed level simulation when M decreases by 60% and W turns from 32% to 98%; (B) Mass fluxes over tidal cycles in recovery stage. Net accreted sediment mass is 2.7 times overestimated without M and W being modified.

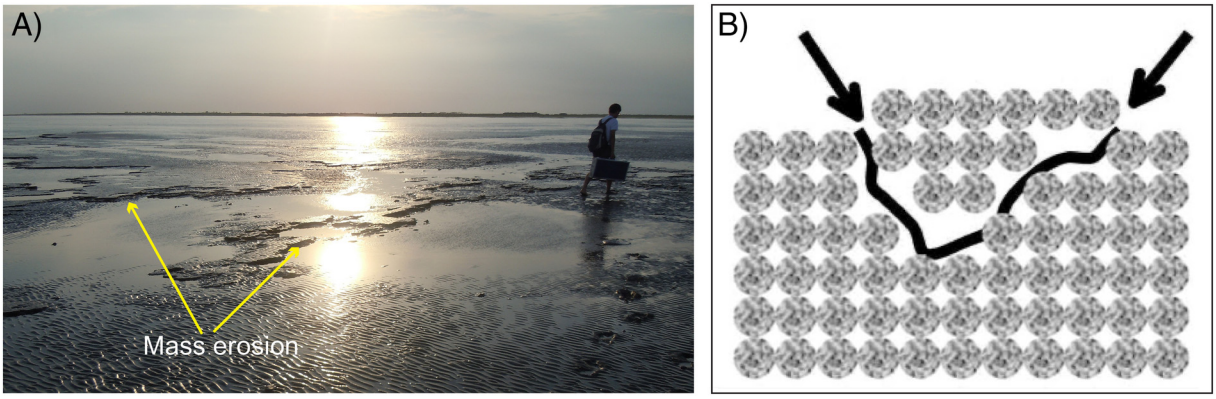

Fig. 11. (A) Photo showing mass erosion on mudflat (taken at 17:30, July 30th); (B) Schematic figure showing mass erosion classified by Winterwerp and van Kesteren (2004, Fig. 9.1d).

Pejrup (2001) found that reworking of the sediment occurred at depth of 3–8 cm. Sediment reworking on shorter temporal scales may be caused by bedform migration (Webster et al., 2013), which is difficult to reproduce in model simulations (Fig. 7D$_1$).

The single-point BLC model employed in this study is unable to solve morphological problems in horizontal scales. For instance, the model fails to describe advection processes, thereby resulting in the SSC variability that further affects deposition rate. However, the erosion and deposition processes described by the model can be embedded into 2D/3D morphological models.

5. Conclusions

We conducted in situ measurements and model simulations on an exposed meso-macrotidal flat on the Yangtze Delta to quantify intertidal bed-level changes under different wind conditions. Bed degradation occurred during periods of strong onshore wind flow, with recovery taking place during subsequent spring tides when the winds were offshore and weaker. Bed recovery was rapid when abundant sediment was delivered by high-energy spring tidal flows. Specifically, such conditions result in increased SSC and enhanced settling through flocculation. Bed recovery is also promoted by tidal asymmetry and sufficient time when τ_{cw} (total bed shear stress) < τ_d (critical shear stress for deposition). The magnitude of bed-level changes during wind events was significantly lower on the salt marsh than on the mudflat. The rapid deposition process greatly affects bed conditions, which further changes the erosion parameters.

The relative importance of waves and tides in the erosion and accretion of intertidal wetlands can vary temporally and spatially. Temporally, tidal force is the dominate factor under weak wind condition, while wave force becomes increasingly important as wind strength increases. Spatially, the degree of wave impact depends on bed elevation and the presence of vegetation that dissipates wave energy. The combination of in situ measurements and numerical simulations used here is an ideal approach for detecting the impact of wind on bed-level changes. The simulated changes in bed level agree well with measured changes when using a single-point BLC (bed level change) model incorporating in situ measured hydrodynamics (waves and currents), SSC, and bed sediment properties. This combined approach also enabled us to assess variability in erosion parameters caused by changes in bed sediment properties during the recovery stage.

Acknowledgements

This study was funded by Natural Science Foundation of China (No. 41576092, 41130856), and The Netherlands Organization for Scientific Research (NWO; Project No. 842.00.007). We thank Benwei Shi, Yingwen Liu, Chuangshou Wu, and Yajuan Li for their assistance in the fieldwork, and Ruiming Wu for his help with grain size analysis. The authors are also grateful to two anonymous reviewers and Editor Prof. Edward Anthony for their constructive suggestions and comments.

Appendix A. Equation Section (Next)Calculation of total bed shear stress τ_{cw}

Total bed shear stress due to combined wave and current action, τ_{cw} (Pa), was calculated using the Grant and Madsen (1979) wave–current interaction model:

$$\tau_{cw} = \sqrt{\left(\tau_w + \tau_c|\cos\varphi_{cw}|\right)^2 + \left(\tau_c|\sin\varphi_{cw}|\right)^2} \tag{A.1}$$

in which τ_w (Pa) and τ_c (Pa) are the wave- and current-induced bed shear stresses, respectively, and φ_{cw} (°) is the angle between current direction φ_c (°) and wave propagation direction φ_w (°). Thus, four separate parameters are required to calculate total bed shear stress: τ_w, τ_c, φ_c, and φ_w.

A.1. Wave-induced bed shear stress

Wave-induced bed shear stress, τ_w, was obtained by analysing surface-elevation monitoring data. Wave parameters (significant wave height H_s and significant wave period T_s) were derived from monitored high-frequency pressure data via linear wave theory (Tucker and Pitt, 2001). At the edge of the wave boundary layer, the peak orbital excursion ($\hat{A}_\delta$) and peak orbital velocity ($\hat{U}_\delta$) can be expressed as:

$$\hat{A}_\delta = \frac{H}{2\sinh(kh)} \tag{A.2}$$

$$\hat{U}_\delta = \omega\hat{A}_\delta = \frac{\pi H}{T\sinh(kh)} \tag{A.3}$$

in which H is wave height (m), k ($=2\pi/L$, $L=(gT^2/2\pi)\tanh(kh)$ is the wave length) is wave number (m^{-1}), h is water depth (m), ω is angular velocity (s^{-1}), and T is wave period (s). In practice, the significant wave height H_s and significant wave period T_s are used for H and T in the formulae.

The time-averaged (over half a wave cycle) bed shear stress due to waves, τ_w (Pa), can be expressed as:

$$\tau_w = \frac{1}{4}\rho_w f_w \hat{U}^2_\delta \tag{A.4}$$

where ρ_w is the water density (kg/m^3) and f_w is the friction coefficient (-), which is determined by the hydraulic regime:

$$f_w = \begin{cases} 2\mathrm{Re}_w^{-0.5} & , \mathrm{Re}_w \le 10^5 \text{ (laminar)} \\ 0.0521\mathrm{Re}_w^{-0.187} & , \mathrm{Re}_w > 10^5 \text{ (smooth turbulent)} \\ 0.237\, r^{-0.52} & , \text{(rough turbulent)} \end{cases} \quad (A.5)$$

in which $\mathrm{Re}_w = \frac{\hat{U}_\delta \hat{A}_\delta}{\nu}$ and $r = \frac{\hat{A}_\delta}{k_s}$ are the wave Reynolds number (-) and relative roughness (-), respectively. Parameter k_s is the Nikuradse roughness value given as $k_s = 2.5d_{50}$, where d_{50} is the median grain size of the bed sediment, and ν is the kinematic viscosity of sea water ($m^2\ s^{-1}$).

A.2. Current-induced bed shear stress

Variability in turbulent velocity fluctuation in the vertical dimension $\overline{w_t^2}$ is used to infer bed shear stress via the following equation (in SI units):

$$\tau_c = C\rho_w \overline{w_t^2} \quad (A.6)$$

in which ρ_w is the sea water density and the constant C is 0.19, after (Stapleton and Huntley, 1995). As high-resolution measurements of near-bed velocity might be affected by surface wave motion, we used wave–turbulence decomposition. Specifically, we used the energy spectrum analysis (ESA) approach, which is a technique developed by (Soulsby and Humphery (1990) to split the variance without separating the instantaneous time series.

A.2.1. Wave and current direction

Current direction φ_c is determined from the arctangent of burst-mean velocities in easterly and northerly orientations, whereas wave direction φ_w is probably determined from the arctangent of wave orbital velocities. The wave orbital velocity is decomposed from wave–turbulent velocities using band-pass filtration, the pass band of which is determined from the wave spectra.

References

Allen, J.R.L., Duffy, M.J., 1998. Medium-term sedimentation on high intertidal mudflats and salt marshes in the Severn Estuary, SW Britain: the role of wind and tide. Mar. Geol. 150, 1–27.

Andersen, T.J., 2001. Seasonal variation in erodibility of two temperate, microtidal mudflats. Estuar. Coast. Shelf Sci. 53, 1–12.

Andersen, T.J., Fredsoe, J., Pejrup, M., 2007. In situ estimation of erosion and deposition thresholds by Acoustic Doppler Velocimeter (ADV). Estuar. Coast. Shelf Sci. 75, 327–336.

Andersen, T.J., Pejrup, M., 2001. Suspended sediment transport on a temperate, microtidal mudflat, the Danish Wadden Sea. Mar. Geol. 173, 69–85.

Andersen, T.J., Pejrup, M., Nielsen, A.A., 2006. Long-term and high-resolution measurements of bed level changes in a temperate, microtidal coastal lagoon. Mar. Geol. 226, 115–125.

Ariathurai, C., 1974. A Finite Element Model for Sediment Transport in Estuaries. University of California, Berkley, USA.

Baas, J.H., Davies, A.G., Malarkey, J., 2013. Bedform development in mixed sand-mud: the contrasting role of cohesive forces in flow and bed. Geomorphology 182, 19–32.

Barbier, E.B., Koch, E.W., Silliman, B.R., Hacker, S.D., Wolanski, E., Primavera, J., Granek, E.F., Polasky, S., Aswani, S., Cramer, L.A., Stoms, D.M., Kennedy, C.J., Bael, D., Kappel, C.V., Perillo, G.M.E., Reed, D.J., 2008. Coastal ecosystem-based management with nonlinear ecological functions and values. Science 319, 321–323.

Bassoullet, P., Le Hir, P., Gouleau, D., Robert, S., 2000. Sediment transport over an intertidal mudflat: field investigations and estimation of fluxes within the "Baie de Marennes-Oleron" (France). Cont. Shelf Res. 20, 1635–1653.

Blum, M.D., Roberts, H.H., 2009. Drowning of the Mississippi Delta due to insufficient sediment supply and global sea-level rise. Nat. Geosci. 2, 488–491.

Christie, M.C., Dyer, K.R., Turner, P., 1999. Sediment flux and bed level measurements from a macro tidal mudflat. Estuar. Coast. Shelf Sci. 49, 667–688.

Chu, Z.X., Sun, X.G., Zhai, S.K., Xu, K.H., 2006. Changing pattern of accretion/erosion of the modern Yellow River (Huanghe) subaerial delta, China: based on remote sensing images. Mar. Geol. 227, 13–30.

Costanza, R., dArge, R., deGroot, R., Farber, S., Grasso, M., Hannon, B., Limburg, K., Naeem, S., Oneill, R.V., Paruelo, J., Raskin, R.G., Sutton, P., vandenBelt, M., 1997. The value of the world's ecosystem services and natural capital. Nature 387, 253–260.

Ding, P., Hu, K., Kong, Y., Hu, D., 2003. Numerical simulation of storm-induced erosion/deposition in Yangtze estuary – a case study of typhoon Jelawat. J. Sediment. Res. 0, 18–24 (in Chinese).

Dyer, K.R., 1986. Coastal and Estuarine Sediment Dynamics. John Wiley & Sons Inc.

Fan, D.D., Guo, Y.X., Wang, P., Shi, J.Z., 2006. Cross-shore variations in morphodynamic processes of an open-coast mudflat in the Changjiang Delta, China: with an emphasis on storm impacts. Cont. Shelf Res. 26, 517–538.

Friedrichs, C.T., 2011. Tidal flat morphodynamics: a synthesis. In: Hansom, J.D., Flemming, B.W. (Eds.), Treatise on Estuarine and Coastal Science. Elsevier.

Gallagher, E.L., Boyd, W., Elgar, S., Guza, R.T., Woodward, B., 1996. Performance of a sonar altimeter in the nearshore. Mar. Geol. 133, 241–248.

Goodwin, P., Mehta, A.J., Zedler, J.B., 2001. Tidal wetland restoration: an introduction. J. Coast. Res. 27, 1–6.

Grant, W.D., Madsen, O.S., 1979. Combined wave and current interaction with a rough bottom. J. Geophys. Res. Oceans Atmos. 84, 1797–1808.

Green, M.O., Black, K.P., Amos, C.L., 1997. Control of estuarine sediment dynamics by interactions between currents and waves at several scales. Mar. Geol. 144, 97–116.

Green, M.O., Coco, G., 2014. Review of wave-driven sediment resuspension and transport in estuaries. Rev. Geophys. 52, 77–117.

Group of Shanghai Coastal Investigation (GSCI), 1988. Report of Shanghai Coastal Comprehensive Investigation. Shanghai Scientific and Technological Press, Shanghai (in Chinese).

Hu, K., Ding, P., Ge, J., 2007. Modelling of storm surge in the coastal waters of Yangtze Estuary and Hangzhou Bay, China. J. Coast. Res. 527–533.

Hu, Z., Wang, Z.B., Zitman, T.J., Stive, M.J.F., Bouma, T.J., 2015. Predicting long-term and short-term tidal flat morphodynamics using a dynamic equilibrium theory. J. Geophys. Res. Earth Surf. 120, 1803–1823.

Jaramillo, S., Sheremet, A., Allison, M.A., Reed, A.H., Holland, K.T., 2009. Wave-mud interactions over the muddy Atchafalaya subaqueous clinoform, Louisiana, United States: wave-supported sediment transport. J. Geophys. Res. Oceans 114.

Jestin, H., Bassoullet, P., Le Hir, P., L'Yavanc, J., Degres, Y., 1998. Development of ALTUS, a High Frequency Acoustic Submersible Recording Altimeter to Accurately Monitor Bed Elevation and Quantify Deposition and Erosion Of Sediments, Oceans'98. pp. 189–194.

Kim, S.C., Friedrichs, C.T., Maa, J.P.Y., Wright, L.D., 2000. Estimating bottom stress in tidal boundary layer from Acoustic Doppler Velocimeter data. J. Hydraul. Eng. ASCE 126, 399–406.

Kineke, G.C., Sternberg, R.W., Trowbridge, J.H., Geyer, W.R., 1996. Fluid-mud processes on the Amazon continental shelf. Cont. Shelf Res. 16, 667–696.

Kirby, R., Bleakley, R., Weatherup, T., Raven, P.J., Donaldson, D., 1992. Effect of episodic events on tidal mud flat stability, Ardmillan Bay, Strangford Lough, Northern Ireland. In: Mehta, A.J. (Ed.), Nearshore and Estuarine Cohesive Sediment Transport. Pacific Rim Congress, Washington, pp. 378–392.

Krone, R.B., 1962. Flume Studies of the Transport of Sediment in Estuarial Shoaling Processes, Final Report Hydraulic Engineering Laboratory and Sanitary Engineering Research Laboratory. University of California, Berkeley, USA.

Lin, C.Y.M., Venditti, J.G., 2013. An empirical model of subcritical bedform migration. Sedimentology 60, 1786–1799.

Lumborg, U., 2005. Modelling the deposition, erosion, and flux of cohesive sediment through Oresund. J. Mar. Syst. 56, 179–193.

Maan, D.C., van Prooijen, B.C., Wang, Z.B., De Vriend, H.J., 2015. Do intertidal flats ever reach equilibrium? J. Geophys. Res. Earth Surf. 120, 2406–2436.

Maire, O., Lecroart, P., Meysman, F., Rosenberg, R., Duchene, J.C., Gremare, A., 2008. Quantification of sediment reworking rates in bioturbation research: a review. Aquat. Biol. 2, 219–238.

McAnally, W.H., Friedrichs, C., Hamilton, D., Hayter, E., Shrestha, P., Rodriguez, H., Sheremet, A., Teeter, A., Flu, A.T.C.M., 2007. Management of fluid mud in estuaries, bays, and lakes. I: Present state of understanding on character and behavior. J. Hydraul. Eng. ASCE 133, 9–22.

Mehta, A.J., McAnally, W.H., 2008. Fine-grained sediment transport. Am. Soc. Civil Eng.

O'Brien, D.J., Whitehouse, R.J.S., Cramp, A., 2000. The cyclic development of a macrotidal mudflat on varying timescales. Cont. Shelf Res. 20, 1593–1619.

O'Shea, M., Murphy, J., 2013. Predicting and monitoring the evolution of a coastal barrier dune system postbreaching. J. Coast. Res. 29, 38–50.

Palanques, A., de Madron, X.D., Puig, P., Fabres, J., Guillen, J., Calafat, A., Canals, M., Heussner, S., Bonnin, J., 2006. Suspended sediment fluxes and transport processes in the Gulf of Lions submarine canyons. The role of storms and dense water cascading. Mar. Geol. 234, 43–61.

Partheniades, E.A., 1965. Erosion and deposition of cohesive soils. World J. Biol. Psychiatry 2, 190–192.

Pejrup, M., 1988. Suspended sediment transport across a tidal flat. Mar. Geol. 82, 187–198.

Postma, H., 1961. Transport and accumulation of suspended matter in the Dutch Wadden Sea. Netherlands Journal of Sea Research]–>Neth. J. Sea Res. 1, 148–190.

Quaresma, V.d.S., Bastos, A.C., Amos, C.L., 2007. Sedimentary processes over an intertidal flat: a field investigation at Hythe flats, Southampton Water (UK). Mar. Geol. 241, 117–136.

Saulter, A.N., Russell, P.E., Gallagher, E.L., Miles, J.R., 2003. Observations of bed level change in a saturated surf zone. J. Geophys. Res. Oceans 108.

Shi, B.W., Wang, Y.P., Yang, Y., Li, M.L., Li, P., Ni, W.F., Gao, J.H., 2015. Determination of critical shear stresses for erosion and deposition based on in situ measurements of currents and waves over an intertidal mudflat. J. Coast. Res. 31, 1344–1356.

Siadatmousavi, S.M., Jose, F., 2015. Winter storm-induced hydrodynamics and morphological response of a shallow transgressive shoal complex: Northern Gulf of Mexico. Estuar. Coast. Shelf Sci. 154, 58–68.

Soulsby, R., Humphery, J., 1990. Field Observations of Wave-current Interaction at the Sea Bed, Water Wave Kinematics. Springer, pp. 413–428.

Stapleton, K., Huntley, D., 1995. Seabed stress determinations using the inertial dissipation method and the turbulent kinetic energy method. Earth Surf. Process. Landf. 20, 807–815.
Taki, K., 2001. Critical shear stress for cohesive sediment transport. In: McAnally, W.H., Mehta, A.J. (Eds.), Coastal and Estuarine Fine Sediment Processes. Elsevier Science, pp. 53–61.
Teisson, C., Ockenden, M., Le Hir, P., Kranenburg, C., Hamm, L., 1993. Special issue coastal morphodynamics: processes and modelling cohesive sediment transport processes. Coast. Eng. 21, 129–162.
Thornton, E.B., Swayne, J.L., Dingler, J.R., 1998. Small-scale morphology across the surf zone. Mar. Geol. 145, 173–196.
Traykovski, P., Geyer, W.R., Irish, J.D., Lynch, J.F., 2000. The role of wave-induced density-driven fluid mud flows for cross-shelf transport on the Eel River continental shelf. Cont. Shelf Res. 20, 2113–2140.
Tucker, M.J., Pitt, E.G., 2001. Waves in Ocean Engineering. Elsevier Ocean Engineering Book Series. vol. 5. Elsevier, Amsterdam.
Turner, I.L., Russell, P.E., Butt, T., 2008. Measurement of wave-by-wave bed-levels in the swash zone. Coast. Eng. 55, 1237–1242.
Van Kessel, T., Kranenburg, C., 1998. Wave-induced liquefaction and flow of subaqueous mud layers. Coast. Eng. 34, 109–127.
Van Prooijen, B.C., Winterwerp, J.C., 2010. A stochastic formulation for erosion of cohesive sediments. J. Geophys. Res. Oceans 115, 15.
Van Straaten, L., Kuenen, P.H., 1958. Tidal action as a cause of clay accumulation. J. Sediment. Res. 28.
Wang, Y.P., Gao, S., Jia, J., Thompson, C.E.L., Gao, J., Yang, Y., 2012. Sediment transport over an accretional intertidal flat with influences of reclamation, Jiangsu coast, China. Mar. Geol. 291, 147–161.
Wang, Z., Van Maren, D., Ding, P., Yang, S., Van Prooijen, B., De Vet, P., Winterwerp, J., De Vriend, H., Stive, M., He, Q., 2015. Human impacts on morphodynamic thresholds in estuarine systems. Cont. Shelf Res., CSR3681
Webster, K.L., Ogston, A.S., Nittrouer, C.A., 2013. Delivery, reworking and export of fine-grained sediment across the sandy Skagit River tidal flats. Cont. Shelf Res. 60, S58–S70.
Whitehouse, R., Soulsby, R., Roberts, W., Mitchener, H., 2000. Dynamics of estuarine muds: a manual for practical applications. Tomas Telford Limited, 1 Heron Quay, London.
Willmott, C.J., Ackleson, S.G., Davis, R.E., Feddema, J.J., Klink, K.M., Legates, D.R., O'Donnell, J., Rowe, C.M., 1985. Statistics for the evaluation and comparison of models. J. Geophys. Res. Oceans 90, 8995–9005.
Winterwerp, J.C., 2007. On the sedimentation rate of cohesive sediment. In: Maa, J.P.Y., S., L.P., Schoellhamer, D.H. (Eds.), Proceedings in Marine Science. Elsevier, pp. 209–226.
Winterwerp, J.C., van Kesteren, W.G.M., 2004. Introduction to the Physics of Cohesive Sediment Dynamics in the Marine Environment. Elsevier Science, Amsterdam, The Netherlands.
Xu, K., Mickey, R.C., Chen, Q., Harris, C.K., Hetland, R.D., Hu, K., Wang, J., 2015. Shelf sediment transport during hurricanes Katrina and Rita. Comput. Geosci. 8.
Yang, S.L., 1991. Impact of wind driven wave on short-period erosion of tidal flat. Mark. Sci. 3, 59–64.
Yang, S.L., Friedrichs, C.T., Shi, Z., Ding, P.X., Zhu, J., Zhao, Q.Y., 2003. Morphological response of tidal marshes, flats and channels of the outer Yangtze River mouth to a major storm. Estuaries 26, 1416–1425.
Yang, S.L., Li, H., Ysebaert, T., Bouma, T.J., Zhang, W.X., Wang, Y., Li, P., Li, M., Ding, P., 2008. Spatial and temporal variations in sediment grain size in tidal wetlands, Yangtze Delta: on the role of physical and biotic controls. Estuar. Coast. Shelf Sci. 77, 657–671.
Yang, S.L., Milliman, J.D., Li, P., Xu, K., 2011. 50,000 dams later: erosion of the Yangtze River and its delta. Glob. Planet. Chang. 75, 14–20.
Yang, S.L., Shi, B.W., Bouma, T.J., Ysebaert, T., Luo, X.X., 2012. Wave attenuation at a salt marsh margin: a case study of an exposed coast on the Yangtze estuary. Estuar. Coasts 35, 169–182.
Yang, S.L., Zhang, J., Zhu, J., Smith, J.P., Dai, S.B., Gao, A., Li, P., 2005. Impact of dams on Yangtze River sediment supply to the sea and delta intertidal wetland response. J. Geophys. Res. Earth Surf. 110.
Zhou, Z., van der Wegen, M., Jagers, B., Coco, G., 2016. Modelling the role of self-weight consolidation on the morphodynamics of accretional mudflats. Environ. Model. Softw. 76, 167–181.
Zhu, Q., van Prooijen, B.C., Wang, Z.B., Ma, Y.X., Yang, S.L., 2016. Bed shear stress estimation on an open intertidal flat using in situ measurements. Estuar. Coast. Shelf Sci. http://dx.doi.org/10.1016/j.ecss.2016.08.028.
Zhu, Q., Yang, S., Ma, Y., 2014. Intra-tidal sedimentary processes associated with combined wave–current action on an exposed, erosional mudflat, southeastern Yangtze River Delta, China. Mar. Geol. 347, 95–106.